Chem Soc Rev

TUTORIAL REVIEW

Scanning tunnelling microscopy of epitaxial nanostructures

Cite this: *Chem. Soc. Rev.*, 2014, **43**, 2226

Matthew S. J. Marshall[ab] and Martin R. Castell[c]

Epitaxial nanostructures have generated a great deal of interest because of the applications in catalysis, photonics and nanoelectronics. To study the structure and electronic properties at the nanoscale, scanning tunnelling microscopy (STM) has proven a very effective technique due to its extraordinarily high spatial resolution. Growth modes of epitaxial nanostructures depend predominantly on the surface free energy of the deposited material, and that of the substrate onto which it is deposited, leading to layer-by-layer or island growth modes. The strain due to lattice mismatch plays an important role in the formation of semiconductor quantum dot islands *via* strain-induced transitions in the morphology of epitaxial nanoislands. Examples of the different growth modes observed with STM are presented in this review within a general framework that uses the surface and strain energies to understand the effects that govern nanostructure shapes. Some self-assembled oxide and metal nanostructures, as well as molecular networks, are also discussed.

Received 11th December 2013

DOI: 10.1039/c3cs60458f

www.rsc.org/csr

Key learning points

(1) The basic theory of scanning tunnelling microscopy, how it operates and some considerations for simulating STM images.
(2) The effects of the surface and interfacial free energies on the growth modes and resulting morphology of nanostructures.
(3) How to include the effect of interfacial strain in understanding the morphology of nanoislands.
(4) Self-assembled oxide nanostructures on the surfaces of some perovskite oxides.
(5) Future directions for using STM to study epitaxial nanostructures.

1. Introduction

The scientific study of nanostructured materials is motivated by the phenomenon that as the size of a material decreases to the nanoscale, properties emerge that are not present in the bulk. This is because of quantum mechanical confinement effects, and also due to an increase in the ratio of the surface area to the bulk. The ability to controllably manufacture materials at the nanoscale has implications for (opto)electronic devices to exploit quantum behaviour, and also for catalysts which can be made more efficient because of the relative increase in surface area. To study nanoscale materials, experimental techniques with high spatial resolution must be used. Of the techniques that have emerged, scanning tunnelling microscopy (STM) has proven to be particularly suitable for the study of epitaxial nanostructures and surfaces. STM is among the most surface sensitive techniques, and facilitates the study of surfaces in real space with atomic resolution. Moreover, it provides valuable information on the electronic structure of the surface, as well as the atomic structure.

In this tutorial review, we introduce STM and through a discussion of some common theoretical approximations provide some considerations for simulating STM images using *ab initio* calculations. We illustrate the different growth modes of epitaxial nanostructures through the use of examples from the literature, first in the context of surface free energies and then by discussing the effects of strain that originates at the nanostructure-substrate interface. Moreover, a discussion on the self-assembly of nanostructures on perovskite oxide materials as studied by STM is provided. Metallic nanostructures, molecular networks, and epitaxial graphene are also discussed. This is intended as an introduction to the field, and as a starting point for further exploration. Our aim is to provide a broad, but not exhaustive review, of STM studies of epitaxial nanostructures and the underlying physical mechanisms involved in their synthesis and characterization.

[a] *Center for Research on Interface Structures and Phenomena, Yale University, New Haven, CT, USA 06520*
[b] *Department of Applied Physics, Yale University, New Haven, CT, USA 06520. E-mail: matthew.marshall@yale.edu*
[c] *Department of Materials, University of Oxford, Parks Road, Oxford, UK OX1 3PH. E-mail: martin.castell@materials.ox.ac.uk*

2. The basics of scanning tunnelling microscopy (STM)

Quantum mechanical tunnelling of electrons occurs when two conductors are brought into close proximity and their quantum mechanical wave functions overlap, allowing electrons to travel between them. Because the electrons travel through an energy barrier, this phenomenon has earned the moniker 'tunnelling'. This is in contrast with classical physics, where electrons would require sufficient energy to surmount the energy barrier. For tunnelling to occur, within a realistic measurement context, the distance between the two conductors is typically between 0.3–1 nm. Scanning tunnelling microscopy (STM) capitalises on the phenomenon of quantum mechanical tunnelling to image a surface with a conductive tip. In this case, the two conductors are the sample surface, and a sharp conductive tip, usually separated by a vacuum gap. Fig. 1 shows a schematic diagram of the physical set-up of an STM with an 'atomically sharp' tip as well as atoms on the surface.

Energy band diagrams are a useful way to understand the different conditions that give rise to electron tunnelling. The energy band diagram of the tip and sample separated by a macroscopic distance is shown in Fig. 2(a), where no tunnelling occurs between the tip and sample. When the tip and sample are brought sufficiently close for tunnelling to occur, as shown in Fig. 2(b), the Fermi levels of the tip and sample equalize. When a positive voltage V_s is applied to the sample, the Fermi level of the sample will shift by eV_s. Electrons then tunnel from the filled states of the tip into the empty states of the sample, as

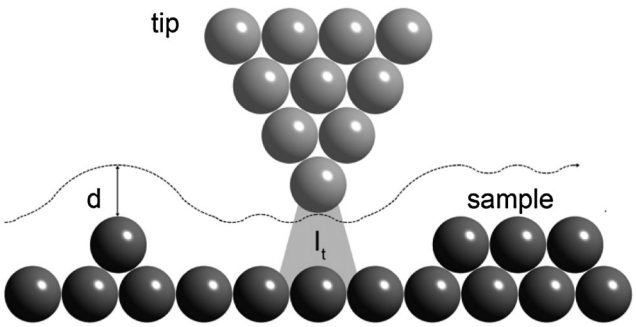

Fig. 1 A schematic showing an 'atomically sharp tip' and the atoms of a surface. The distance between the apex of the tip and the sample surface is labelled *d*, and the tunnelling current is shown as I_t. The dashed line represents the path traced by the apex of the tip while maintaining a constant tunnelling current. This line corresponds to the trace of the atomic topography in the STM image. Image adapted from ref. 1.

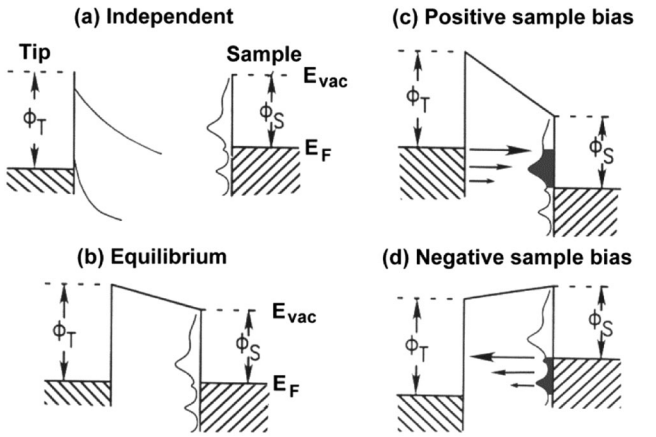

Fig. 2 Energy band diagrams for the STM tip and sample. (a) The tip and sample are separated by a macroscopic distance and do not interact; the vacuum level is the same for both the tip and the sample. (b) The tip-sample distance is within tunnelling range and the system has reached equilibrium. Applying a positive voltage to the sample, as in (c), causes electrons to tunnel from filled tip states into empty sample states. In (d), a negative sample voltage means that electrons tunnel from filled sample states to empty tip states. Adapted from Hamers.[2]

Matthew S. J. Marshall

Matthew S. J. Marshall received a BASc in Engineering Science from the University of Toronto in 2005. He obtained his DPhil in 2009 from Oxford University for his work using ultra-high vacuum scanning tunneling microscopy to study nanostructured strontium titanate surfaces. He is currently a postdoctoral associate in the Dept. of Applied Physics at Yale University and a member of the Center for Research on Interface Structures and Phenomena (CRISP), where he uses oxide molecular beam epitaxy to develop materials systems for novel electronic devices.

Martin R. Castell

Martin R. Castell completed his PhD in Physics in 1994 at the University of Cambridge. He then moved as a Junior Research Fellow to the Department of Materials at the University of Oxford. From 1999 he held a Royal Society University Research Fellowship, followed in 2005 by a University Lectureship, and was made a Professor in 2010. He has held visiting positions at the University of Toronto, Queen's University Belfast, and the University of New South Wales. His main research activity is using UHV scanning tunneling microscopy to investigate the atomic structure of oxide crystal surfaces, ultra-thin films, and nanostructures.

shown in Fig. 2(c). Conversely, when a negative voltage is applied to the sample, electrons tunnel from the filled states of the sample into the empty states of the tip, as shown in Fig. 2(d). The important implication of this is that both the empty and filled states of the sample can be imaged with STM, and voltage *versus* tunnelling current spectroscopy can be performed. These spectroscopic measurements are related to the local density of electronic states of the sample. Because STM images are a convolution of the atomic and electronic surface structure, comparisons with *ab initio* image simulations are invaluable for facilitating interpretation of complex experimental STM images. This requires approximating the tunnelling current in a manner that can be modelled with first principles density functional theory (DFT).

While numerous treatments of the theory of STM have been developed, the Tersoff–Hamann approximation is the most widely-used.[3] It assumes that the structure of the tip is unknown, and that it therefore can be approximated as a spherical potential well, with tunnelling occurring through asymptotic s-states located at the apex of the tip. To facilitate the development of an analytical solution, it is further assumed that the work functions of the tip and sample are approximately equal. In the limit of small applied bias voltages and low-temperature, the tunnelling current can be expressed in terms of the position and energy-dependent local density of electronic states (LDOS) of the surface $\rho_s(\boldsymbol{r}, E_F)$:

$$\rho_s(\boldsymbol{r}, E_F) = \sum_{\mu} \left|\psi_\mu(\boldsymbol{r})\right|^2 \delta(\varepsilon_\mu - E_F) \quad (1)$$

where E_F is the Fermi level, and ψ_μ is the sample wave function with an eigenvalue of ε_μ. The tunnelling current, I_t, can then be written in terms of the LDOS:

$$I_t \propto \int_0^{eV_b} \rho_s(\boldsymbol{r}, E_F + \varepsilon) d\varepsilon \quad (2)$$

$$I_t \propto e^{-2\kappa d} \int_0^{eV_b} \rho_s(E_F + \varepsilon) d\varepsilon \quad (3)$$

where d is the distance between the sample and the tip, and $\kappa = \sqrt{(2m_e\varphi)}/\hbar$ where m_e is the mass of the electron, φ is the work function of the tip, and V_b is the bias voltage applied to the sample. If we estimate the work function to be φ = 4 eV, then $\kappa \approx 1$ Å^{-1}. Under this approximation, we see that when the distance between the tip and the sample increases from 3 Å to 5 Å, the tunnelling current decays to less than 2% of the original value.

Using the approximation described by eqn (1)–(3), STM images can therefore be modelled using *ab initio* calculations by integrating over an energy window to produce a map of the local density of electronic states. This approximation works best for metallic samples and breaks down above bias voltages of about 100 mV. However, the Tersoff–Hamann approximation can be modified to include high-bias voltages and non-spherical tip states following Stokbro *et al.*,[4] using the tip wave function expansion described by Chen.[5] This modified approach for approximating the tunnelling current in the high-bias voltage limit, V_b, is therefore:[6]

$$I_t \propto \int_{E_F}^{E_F+eV_b} \kappa(\varepsilon)^{-2} \rho_s(\boldsymbol{r}, \varepsilon) d\varepsilon \quad (4)$$

where

$$\kappa(\varepsilon) = \hbar^{-1}\sqrt{2m_e(\varphi_t + E_F + eV_b - \varepsilon)} \quad (5)$$

is the inverse decay length of electron states into the vacuum for an energy ε, φ_t is the work function of the tip, m_e is the mass of an electron and e is the charge on an electron. To implement the high-bias approach using DFT in order to simulate STM images, the unoccupied states between E_F and $E_F + eV_b$ must be artificially populated, and weighted with a factor $\kappa(\varepsilon)^{-2}$, as contained within eqn (4) and (5). For more thorough theoretical treatments of the theory that underpins STM see Chen,[5] and Wiesendanger.[7]

In practice, the experimental STM apparatus functions in one of two measurement modes: constant current mode, and constant height mode. Constant height mode maintains the z-position of the tip as it scans across the surface, while constant current mode maintains a user-defined set-point current by continuously adjusting the tip-sample separation. Constant current mode has a higher z-range, and as such, is less likely to suffer tip crashes. This is particularly important for a nanostructured surface that has a large height variance. Both imaging modes require accurate control of the tip and sample position, which is achieved using piezoelectric crystals. Applying a saw-tooth voltage to the piezoelectric crystal raster scans the tip across the surface.

3. Introduction to epitaxial growth of nanostructures

Fabricating nanoscale features using lithographic processes is challenging, as evidenced by the work to avoid the end of Moore's Law. The most extreme example of nanoscale fabrication is the work performed in Eigler's group who used STM to move individual atoms around one-by-one to create a quantum corral on the surface of Cu(111), providing a vivid illustration of quantum confinement, as manifested by the ripples in the LDOS.[8] Their approach of moving atoms one at a time, while a technological marvel, is impractical for making extended nanostructures or devices due to the length of time it would take. An alternative is to instead use intermolecular and interatomic forces to create desired nanoscale features. Nanostructures consist of atoms, clusters of atoms, and molecules. The formation of epitaxial nanostructures is dictated by the energetics of the interactions between these building blocks, and with the substrate upon which they are grown. The simplest interaction is the formation of crystals from atoms evaporated onto a substrate, when provided with sufficient thermal energy to condense into a crystal.

When considering the formation of epitaxial nanostructures two factors must be considered. The first is the energetics of the surface and of the nanostructure. The second is the strain

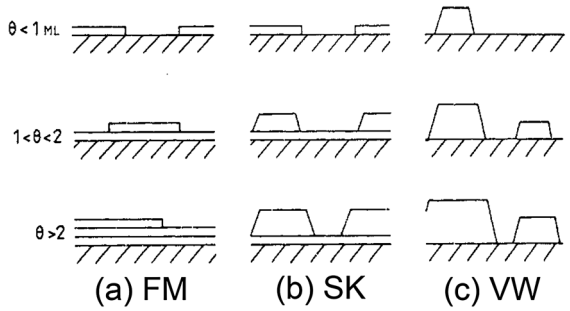

Fig. 3 Schematic illustrations of the evolution of the three main film growth modes as a function of monolayer (ML) surface coverage θ. (a) Layer-by-layer film growth called Frank–van der Merwe (FM) growth. (b) Layer-by-layer growth followed by island formation called Stranski–Krastanov (SK) growth (c) Island formation called Volmer–Weber (VW) growth. Adapted from Venables *et al., Rep. Prog. Phys.*, 1984.[10]

energy, where the strain is determined by the lattice mismatch between the nanostructure and the substrate material. The energetics of the surface, as defined by the surface free energies, play a crucial role in epitaxy. The surface free energies are closely related to the interaction strength between an atom and the substrate during growth. This results in three distinct growth regimes called: (a) layer-by-layer or Frank–van der Merwe (FM) growth; (b) layer-by-layer followed by islanding or Stranski–Krastanov (SK) growth; (c) island formation or Volmer–Weber (VW) growth. The three growth modes as a function of surface coverage, θ, are shown in Fig. 3.

Volmer–Weber (VW) growth occurs for situations where the interatomic interactions between the adatoms are stronger than between the adatoms and the substrate. The result is that the adatoms cluster together to create 3D islands, as shown in Fig. 3(c). As more adatoms are added, the islands grow larger. An alternative way of viewing the same situation is to say that the surface energy of the substrate is less than the sum of the surface energy of the film and the interface energy *i.e.* $\gamma_{substrate} < \gamma_{film} + \gamma_{interface}$.

Conversely, when the inequality above is reversed *i.e.* $\gamma_{substrate} > \gamma_{film} + \gamma_{interface}$, then 2D Frank–van der Merwe (FM) growth results, as shown in Fig. 3(a). The initial monolayer (ML) of adatoms that are deposited on the substrate have a larger interaction strength with the substrate than with each other. This results in 2D growth, and the film is said to 'wet' the surface. As more adatoms impinge on the substrate the film builds up in a layer-by-layer fashion.

A significant variant of FM growth is called Stranski–Krastanov (SK) growth. In this regime the interfacial and surface energies favour FM growth, and this is what is observed in the initial stages of film growth. However, if the growing film is strained due to misfit between the lattices of the substrate and the film, then strain energy is incorporated into the film in proportion to its thickness. Beyond a critical thickness the strain energy becomes large enough to initiate one of a number of possible strain relieving mechanisms. The two most common are the introduction of misfit dislocations at the film-substrate interface and the transition to 3D island growth. SK growth, shown schematically in Fig. 3(b), is the situation where the film initially wets the substrate but then after a certain thickness transitions to 3D growth. In Fig. 3(b) the critical thickness is a single monolayer, but in many SK systems the critical thickness can be much greater. Misfit dislocations may additionally also be present in SK growth systems.[9]

4. Nanoisland formation studied with STM

4.1 3D nanoislands formed *via* Volmer–Weber growth

STM is adept at probing the growth of small islands on top of a conducting substrate. Such nanoislands mainly form *via* the Volmer–Weber growth mode, in which islands with relatively high surface free energies form atop a lower energy substrate. The shape of the nanoislands largely depends on the energy of the island facets, the energy of the interface between the substrate and island, as well as that of the substrate. Insight into the nanoisland morphology can be gained from calculating the equilibrium minimum energy shape using the modified Wulff construction.[11]

The Wulff construction is a powerful conceptual tool facilitating an easy derivation of the equilibrium shape of a free-standing crystal. Defined in terms of the Gibbs free energy, ΔG, it is an energy minimization defined as $\Delta G = \Sigma(\gamma_j A_j)$ where γ_j is the energy of surface facet with area A_j. The crystallographic orientation that minimizes the total surface and interface energy of the nanoisland therefore dictates its shape. The Wulff construction is created on a 3D polar plot where a line, $\boldsymbol{n}_{hkl}$, of length, γ_{hkl}, is drawn perpendicular to each crystallographic orientation.[13] At the end of the lines, each of length γ_{hkl}, a perpendicular plane is drawn. A Wulff construction is the shape that is enclosed by these planes, which defines the Wulff shape.[12] For a crystal grown on a substrate there is also an equilibrium shape that can be determined through the modified Wulff construction. For supported crystals the energy minimisation is $\Delta G = \Sigma(\gamma_j A_j) + \gamma_i A_i - \gamma_s A_i$ where γ_i, γ_s, A_i are the interfacial and substrate energies and area, respectively. It can be experimentally challenging to determine the surface energies necessary for the Wulff construction, and so *ab initio* calculations performed using DFT can be used to furnish values for the surface energies.

The effects of surface and interface energies on the shape of nanoislands can be shown through the example of Pd on $SrTiO_3(001)$, as studied with STM.[14] Depositing Pd onto $SrTiO_3$ under different conditions leads to the formation of three different island shapes. Pd is closely lattice matched to $SrTiO_3$, facilitating commensurate and coincident epitaxial growth. Commensurate epitaxy occurs when all lattice points in the over-layer are matched to points on the substrate, whereas coincident epitaxy is when only some of the lattice is matched between the substrate and over-layer. Depending on the reconstruction of the substrate, the temperature at which Pd is deposited, and the post-growth annealing temperature, three types of islands are formed: flat hexagonal nanocrystals, truncated pyramids and hut cluster structures. For island shapes

that have a constant ratio of length to height as a function of island volume, the equilibrium shape has been reached, as is the case for truncated pyramids and hut clusters. However, the hexagonal islands are in a metastable state and the width to height ratio is not constant as a function of volume. Analysis of the island dimensions provides insight into the relative energies of the island facets, substrate, and interfaces. In this instance, the variation in substrate surface energy due to the different surface reconstructions determines which Pd nanocrystal shape is energetically most stable.

The observed island shapes are analysed using the modified Wulff construction for Pd on $SrTiO_3(001)$ as shown in Fig. 4. An STM image showing the truncated pyramid nanoislands is shown in Fig. 5, with the inset showing a high resolution 3D rendering of the Pd nanoislands. Surface energies derived using first principles calculations are used as a basis for the Pd facet energies. This analysis reveals that the reconstructed substrate surface energy is critically important in determining the final shape. Controlling the shape of nanoislands of noble metals such as Pd is particularly important because of its use as a catalyst.

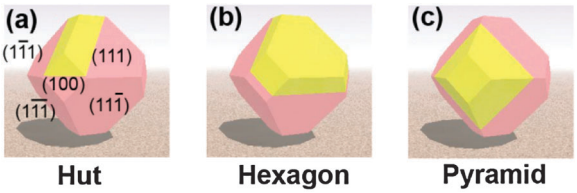

Fig. 4 Equilibrium shape of a Pd nanoparticle. The yellow segments demonstrate how different crystallographic interfaces result in different island shapes (a) a (110) interface results in a hut shape, (b) a (111) interface causes and hexagonal shape, and (c) a (100) interface gives rise to a truncated pyramid shape. Reprinted figure with permission from [F. Silly and M. R. Castell, *Phys. Rev. Lett.*, 2005, **94**, 046103]. Copyright (2005) by the American Physical Society.[14]

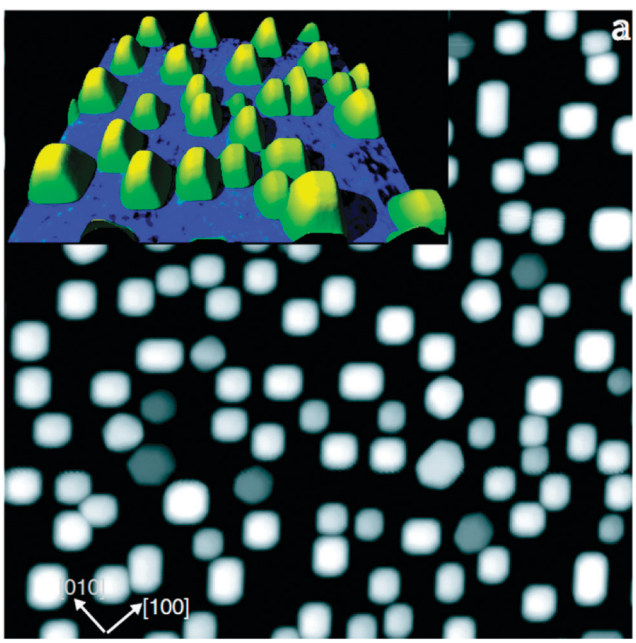

Fig. 5 STM image showing Pd truncated pyramids, as seen in Fig. 4(c), on $c(4 \times 2)$ $SrTiO_3(001)$ (140 × 140 nm^2; V_s = + 0.8 V, I_s = 0.3 nA), with a high magnification 3D rendering inset. Reprinted figure with permission from [F. Silly and M. R. Castell, *Phys. Rev. Lett.*, 2005, **94**, 046103]. Copyright (2005) by the American Physical Society.[14]

4.2 2D nanoislands formed by Frank–van der Merwe growth

STM images are a convolution of the topography of the structure and the local density of electronic states (LDOS). This can be exploited to probe highly spatially localized LDOS. For small particles in which the LDOS is important, STM facilitates the correlation of atomic and electronic structure. One notable example is the study of MoS_2 nanoclusters grown on reconstructed Au substrates. MoS_2 is chemically inactive in the bulk, but is catalytically active at small length scales. It has proven useful as a catalyst for hydrogenation of aromatic compounds, as well as in hydrotreating catalysis – the hydrogenolysis of sulphur from an organic compound.[15]

To study MoS_2 using scanning tunnelling microscopy, physical vapour deposition has been used to deposit clusters of Mo on an inert Au(111) substrate. The Au(111) surface adopts a herringbone reconstruction due to $(\sqrt{3} \times 22)$ ordering which has a regular distribution of 60° elbows. During the deposition of Mo, clusters nucleate at these elbows, resulting in an even distribution of flat Mo clusters across the surface, as shown Fig. 6(a), with the herringbone reconstruction visible around the nanoclusters. The Mo clusters are annealed in a sulphur atmosphere to form MoS_2 nanoclusters that are one monolayer thick, an example of which is shown in Fig. 6(b) which displays atomic resolution with a bright edge state visible surrounding the island. These nanostructures are FM type nanoislands, and because they are one monolayer thick can be considered '2D' nanostructures. The 2D Wulff construction for MoS_2 is shown inset in Fig. 6(b). When the atomic termination of the edge are Mo atoms, the edge has an

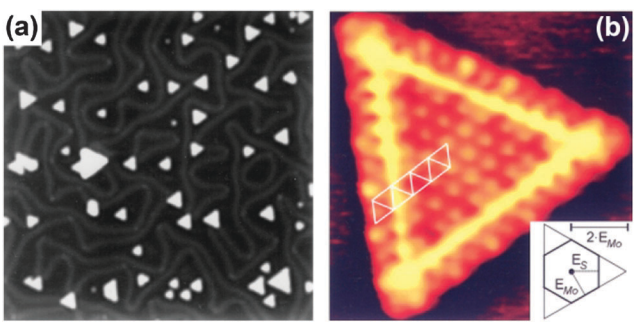

Fig. 6 STM images showing MoS_2 nanoclusters on an Au(111) surface. Panel (a) shows the distribution of clusters (74 × 72 nm^2), and panel (b) is a close-up of one cluster showing atomic resolution with a bright edge state visible (41 × 42 $Å^2$, I_t = 1.28 nA and V_t = 5.2 mV). Inset in (b) is the 2D Wulff construction, where E_{Mo} refers to the energy for Mo atoms at the edge and E_S refers to S atoms at the edge. Reprinted figure with permission from [S. Helveg *et al.*, *Phys. Rev. Lett.*, 2000, **84**, 951–954]. Copyright (2000) by the American Physical Society.[16]

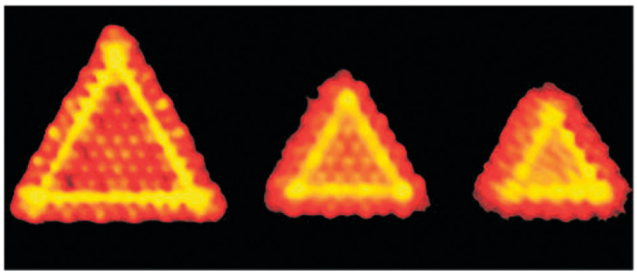

Fig. 7 STM images of three MoS_2 nanoclusters ($Mo_{78}S_{204}$, $Mo_{36}S_{104}$, $M_{28}S_{84}$). The edges have 12, 8, and 7 Mo atoms, respectively. The odd number of Mo atoms along the edge is energetically disfavoured compared to even numbers of Mo edges. The atomic structure is visible in these images, as well as the bright metallic edge state. Reprinted by permission from Macmillan Publishers Ltd: [*Nature Nanotechnology*] J. V. Lauritsen *et al.*, *Nat. Nanotechnol.*, 2007, **2**, 53.[15]

energy of E_{Mo}, whereas when it is terminated with S atoms, it has an energy E_S. Because E_{Mo} is much less than E_S, the shape of the island is triangular in order to maximize the length of edges that are terminated with Mo and minimize the total energy of the structure. Hence, an island with Mo atoms at the edge is triangular in shape in the STM images.

The practical application of MoS_2 nanoclusters is in catalysis, particularly desulphurization. In this area, STM enables unique insight into the origins of the catalytic properties. Clearly visible in the STM images shown in Fig. 6 is a bright yellow line along the perimeter of the triangular island. This bright line corresponds to a localized metallic state on an otherwise bulk insulator. These localized metallic states form along the perimeter of monolayer-thick MoS_2 islands and functionally are closed metallic wires. Because these metallic states form along the perimeter, or edge of the island, they are known as edge states. The metallic nature of the edge states are the source of the catalytic behaviour in the nanoclusters, allowing electrons to be donated or accepted.

The size of the MoS_2 nanoclusters also affects the properties, with three differently sized clusters shown Fig. 7. Below a critical size the metallic edge state disappears and the nanocluster becomes entirely semiconducting, losing its catalytic properties. Using a combination of DFT and STM to probe the size of the MoS_2 nanoclusters reveals that the nanoclusters tend to form with an even number of Mo atoms along the edges. This is, in part, because the sulphur tends to dimerise in S_2 as part of a pair-wise reconstruction, and an odd number of Mo atoms would result in unpaired S atoms. These studies indicate that there is likely an optimal nanocluster size for catalysis. The use of STM is crucial in the study of the nanoclusters because of its ability to provide a topographic map of the LDOS, thereby identifying the origin and location of the catalytic activity. For further discussion of using STM to study catalytically relevant systems, refer to Vang *et al.*[17]

4.3 Stranski–Krastanov nanostructures

Examples of nanostructure formation *via* VW and FM growth involving 3D and 2D islands decorating a surface were discussed in the previous two sections. SK growth involves the formation of nanoislands atop a wetting layer with nanoisland formation usually driven by misfit strain between the substrate and the film. There has been a focus on using SK growth to create self-assembled quantum dots with narrow size distributions that could be useful for technological applications. The prototypical example of the SK growth mode is Ge deposited onto Si(001).[18] Initially, Ge deposited onto Si wets the surface forming a uniform layer of Ge. However, the lattice mismatch of 4% between Ge and Si causes strain energy to build up in the Ge layer. This strain is relieved *via* the formation of small islands. Other notable examples of SK growth are GaN on AlN,[19] InAs on GaAs,[20] and Ag on Au(111).[21]

There is a rich field of study that focuses on what happens after the nanoislands nucleate and increase in volume. Nanoislands of pure Ge grown on Si(001) undergo a size-dependent shape transition, at a size that is suitable for study with STM.[22] In Fig. 8(a), the bimodal distribution of small pyramids and larger domes can be seen in the STM image. Notably, a high magnification image shows the atomic structure of the (105) side facets of a pyramid, shown in Fig. 8(b). These images demonstrate the unique capability of the STM to image the surface topography of nanostructures with atomic resolution.

While the simple SK description is approximately correct, it does not capture all the complexities of nanoisland growth, which include kinetic and thermodynamic considerations.[23,24] Once islands have nucleated there is a large body of work that describes the size-dependent shape transitions that the islands undergo. Fig. 9 shows the evolution from small 'pre-pyramid' clusters, to full pyramid clusters that showcase almost entirely (105) side facets, to larger dome and barn shapes, with atomic resolution of the island structure visible most clearly in the pyramid structure shown in Fig. 9(c). These shape transitions depend on the volume of the island, the misfit strain (a function of the ratio of Si : Ge deposited onto the substrate), as well as the growth temperature and post-growth processing conditions. Moreover, the simple free energy description of the surface and interface energies is in fact, more complicated for Ge on Si(001). The surface free energies for the facets of the Ge islands have a strain dependency and as such the surface energy at the base of the island is different than that closest to the apex of the island.[25] These factors must be taken into consideration to fully understand the island growth.

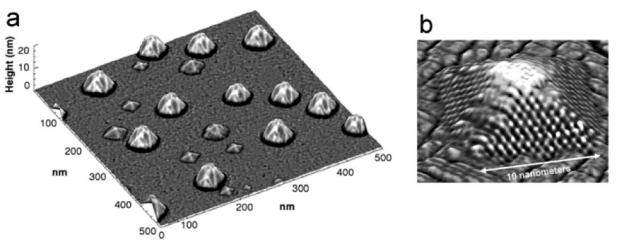

Fig. 8 STM images of Ge nanocrystals on Si(001). (a) The two crystal shapes that can be seen are small pyramids and larger domes. (b) A high magnification image of a single pyramid in which the atomic structure of the (105) side facets is resolvable. From [G. Medeiros-Ribeiro *et al.*, *Science*, 1998, **279**, 353–355]. Reprinted with permission from AAAS.[22]

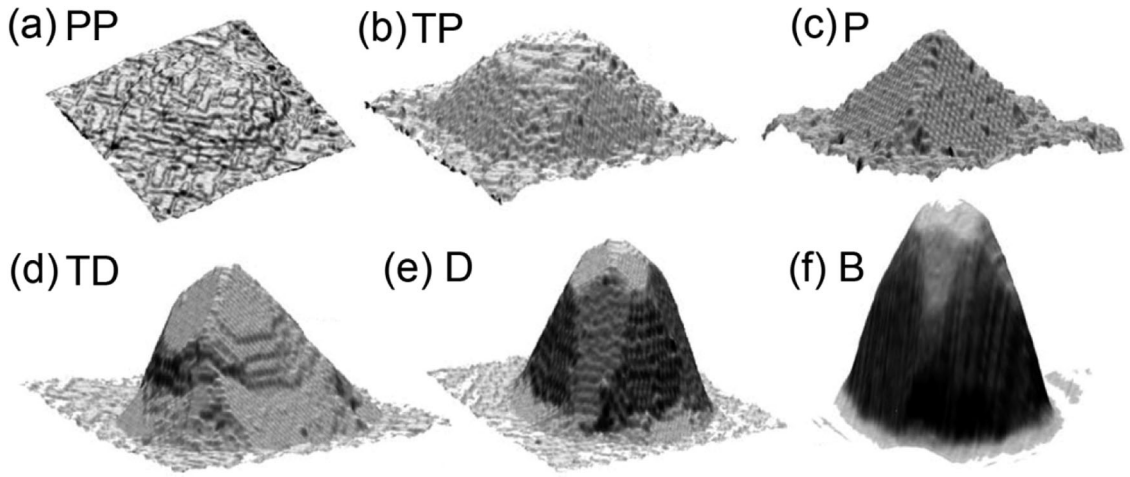

Fig. 9 STM images showing the evolution of coherently strained islands of $Si_{1-x}Ge_x$ on Si(001). A pre-pyramid shape is shown in (a), with a truncated pyramid in (b) and a full pyramid in (c). The pyramid shape evolves into an intermediate truncated dome structure in (d) and full dome structure in (e). An atomic force microscopy (AFM) image of a 'barn' nanoisland is shown in (f). Reprinted from A. Rastelli *et al.*, *Microelectronics Journal*, 2006, **37**, 1471–1476, Copyright (2006), with permission from Elsevier.[26]

5. Effect of strain on epitaxial nanostructures

Thus far, this review has emphasized surface and interface energy considerations in determining the morphology of a nanostructure. In the preceding section, the effect of strain on the growth of epitaxial nanoislands of $Si_{1-x}Ge_x$ on Si(001) demonstrated that misfit strain is relieved *via* the formation of small nanoislands atop a wetting layer, and that these nanoislands undergo shape transitions as they increase in volume. The shape transitions of $Si_{1-x}Ge_x$ nanoislands decorating an Si(001) surface is well described by the Li, Liu, and Lagally (LLL) model that found that huts of $Si_{1-x}Ge_x$ formed adjacent to pits on the surface and were limited by an equilibrium ratio of the width to length. The formation of a pit adjacent to the island creates an anisotropy in the edge energy, therefore lifting the directional degeneracy.[27,28] Including kinetic complexities demonstrated that the formation of the pits has a temperature dependence, below which pits do not form adjacent to the clusters, and therefore no anisotropy is introduced into the edge energy.

5.1 Strain-induced shape evolution of epitaxial strained islands

As is the case for strain-induced shape transitions of epitaxial islands of $Si_{1-x}Ge_x$ on Si(001), misfit strain between VW type islands and their substrates also builds up as the volume of the island increases. This strain can be relieved *via* an alternative mechanism, which is a strain-induced change in island shape. A seminal work in describing the strain-induced shape transition of quantum wires was the work by Tersoff and Tromp.[29] This work is broadly applicable to different materials systems, inasmuch as it is a general theoretical treatment of how strain induces a shape transition. While the original work focused on a strain-induced shape transition from a square cluster to a rectangle, subsequent work has demonstrated that the model also accurately predicts the point at which a shape transition to an irregular shape occurs.[30] While the model is typically for dislocation-free growth, it can easily be adapted for the situation of partial relief of strain by dislocations.

In a simple growth scheme that focuses on the surface free energy of the system, the strain energy is included in the interface term γ_i. However, as the strain energy increases more rapidly with volume than the surface or interface energy a shape transition can be induced. Beyond a critical volume of square shaped island or cluster, the strain is relieved by elongation of the island and a reduction in width. This either occurs by the formation of long narrow rectangles, or by the formation of irregular narrow features. A widely accepted approach for deriving the energy of relaxation was initially applied to periodic domains and equilibrium crystal shapes.[31,32] The approach to deriving the energy of relaxation for a nanoisland uses continuum elasticity theory, as described by Landau and Lifshitz,[33] which led to the Tersoff and Tromp formulation.[29]

The theoretical basis for the strain-induced shape transitions is often referred to in the literature, but the derivation is rarely shown and a fuller discussion is both fruitful and merited. The following derivation is adapted from Marshall.[34] The Tersoff–Tromp approach describes a flat-topped island of width, s, length, t, height, h, and a substrate/island angle of θ, as shown in Fig. 10. The island is not in its thermodynamic equilibrium shape, but rather has its height artificially limited and fixed. This situation is representative of many scenarios where the kinetics of growth result in limited island heights. The total energy of the nanoisland takes the form:

$$E_t = E_s + E_r \quad (6)$$

where E_t is the total energy, E_s is the energy of the surfaces, and E_r is the relaxation energy of the crystal and substrate.

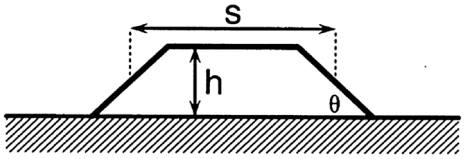

Fig. 10 A schematic of a flat topped island of width, s, length, t, and height, h with a substrate-island angle of θ. Reprinted figure with permission from [J. Tersoff and R. M. Tromp, *Phys. Rev. Lett.*, 1993, **70**, 2782–2785]. Copyright (1993) by the American Physical Society.[29]

The surface energy of the crystal structure depicted in Fig. 10 is therefore given by:

$$E_s = st(\gamma_i + \gamma_t - \gamma_s) + 2(s + t)[h\gamma_e \csc\theta - h\cot\theta(\gamma_t + \gamma_s - \gamma_i/2)] \quad (7)$$

where γ_e, γ_t, γ_s, γ_i are the edge, island top, substrate and interface energies, respectively, with the parameters s, t, h, and θ described in Fig. 10. To obtain the relaxation energy, E_r, the force density on the surface is multiplied by the displacement of the material. The expression for the relaxation energy term, E_r, is therefore:[28]

$$E_r = \int d^2\rho\, f_i(\rho)\, u_i(\rho) \quad (8)$$

where the force density, f_i, depends on how the surface stress is modelled, and the displacement $u_i(\rho)$ is derived using continuum elasticity theory where ρ and ρ' are two dimensional position vectors on the surface, where $\rho = (x, y)$.[33] The displacement in response to an applied force (in this case the stress or strain) is given by:

$$u_\alpha = \int d^2\rho' \chi_{\alpha\beta}(\rho - \rho', z)\, f_i(\rho') = \int d^2\rho d^2\rho' \chi_{\alpha\beta}(\rho - \rho', z)\, f_i(\rho')\, f_j(\rho') \quad (9)$$

where $\chi_{\alpha\beta}$ is the Green's function for an elastic medium, $f_i = \partial_j\sigma_{ij}$, ρ, and u_i have been defined previously.[33] The term, σ_{ij}, is the two dimensional island stress tensor given by $\sigma_{ij} = \sigma_b \times h\delta_{ij}$, where h is the height at any point on the island, and σ_b is equal to the stress in either the xx, or yy directions for a uniformly strained island. Landau gives the Green's function, $\chi_{\alpha\beta}$ for a homogenous and isotropic medium in equilibrium, bounded by a semi-infinite plane with zero stresses at the surface ($z = 0$) as:[35]

$$\chi_{\alpha\beta} = \frac{1}{4\pi\mu}\left[\frac{\delta_{\alpha\beta}}{\rho} - \frac{1}{4(1-\nu)}\frac{\partial^2\rho}{\partial x_\alpha \partial x_\beta}\right] \quad (10)$$

where $\chi_{\alpha\beta}$ is the Green's function, μ is the shear constant of the island, ν is Poisson's ratio of the island, and ρ is the position vector. To solve for E_r it must be assumed that there is no variation in the z-direction within the crystal and that the stress in the z-direction is equal to zero. This gives an expression for E_r:

$$E_r = -\frac{1}{2}\int d\rho d\rho' \chi_{ij}(\rho - \rho') f_i(\rho) f_j(\rho') \quad (11)$$

where corner effects are neglected. Solving for the elastic relaxation energy can be complicated, and is most easily accomplished in reciprocal space. Thus, assuming a homogenous isotropic material bounded by a semi-infinite plane, the relaxation energy is E_r:

$$E_r = -2ch^2\left[s\ln\left(\frac{t}{\phi h}\right) + t\ln\left(\frac{s}{\phi h}\right)\right] \quad (12)$$

where the constant $c = \sigma_b^2(1 - \nu)/2\pi\mu$ and μ, ν and σ are the shear modulus, Poisson's ratio and bulk stress respectively, while $\phi = \cot\theta\, \exp(-3/2)$, with θ defined as the angle between the island edge and the substrate. The total strain and surface/interface energy per unit volume for epitaxially strained islands with kinetically limited height can ultimately be given by the following equation:

$$\frac{E}{V} = 2\Gamma\left(\frac{1}{s} + \frac{1}{t}\right) + \frac{1}{h}(\gamma_i + \gamma_t - \gamma_s) - 2ch\left[\frac{1}{s}\ln\left(\frac{s}{\phi h}\right) + \frac{1}{t}\ln\left(\frac{t}{\phi h}\right)\right] \quad (13)$$

where $\Gamma = \gamma_e \csc\theta - 1/2(\gamma_t + \gamma_s - \gamma_i)\cot\theta$ and γ_e, γ_t, γ_s, γ_i are the edge, island top, substrate and interface energies, respectively. The island width is denoted by s and the length by t. Minimizing the energy of an island of constant height with respect to both the length and width gives the optimal size of the island, where $s = t = \alpha_0$, and is given by:

$$\alpha_0 = e\phi h\, \exp(\Gamma/ch) \quad (14)$$

At the critical point, $e\alpha_0$ the shape transition begins. This transition is illustrated in the scanning electron micrograph (SEM) shown Fig. 11 for epitaxial islands of the anatase polymorph of TiO_2 that form on top of $SrTiO_3(001)$. At a critical size $e\alpha_0$ = 1.3 μm, the shape transforms from squares islands to thinner rectangular islands.[30] The islands of anatase have a low-energy (4 × 1) reconstruction that produces flat-topped truncated pyramids, with the pyramid top corresponding to the (001) orientation of anatase.[36] As the islands transform from squares into long, thin rectangles it becomes difficult to capture the length of the island in a single STM image, thereby necessitating the use of scanning electron microscopy, or in the original work by Tersoff and Tromp low-energy electron microscopy (LEEM).[29]

This formalism is for isotropically strained islands. Anisotropic strain will favour a particular direction of elongation. Preferential orientation was observed for islands of Ag on the (4 × 1) reconstruction of Si(111).[37] The lattice mismatch between Ag and Si(111) induces a shape transition as the volume of the Ag clusters increases, but because the anisotropic nature of the strain between the nanoislands and the Si reconstruction lifts directional degeneracy, the nanoislands all elongate in the same direction. This is shown in Fig. 12 where numerous Ag nanoislands of similar width are all oriented in the same direction.

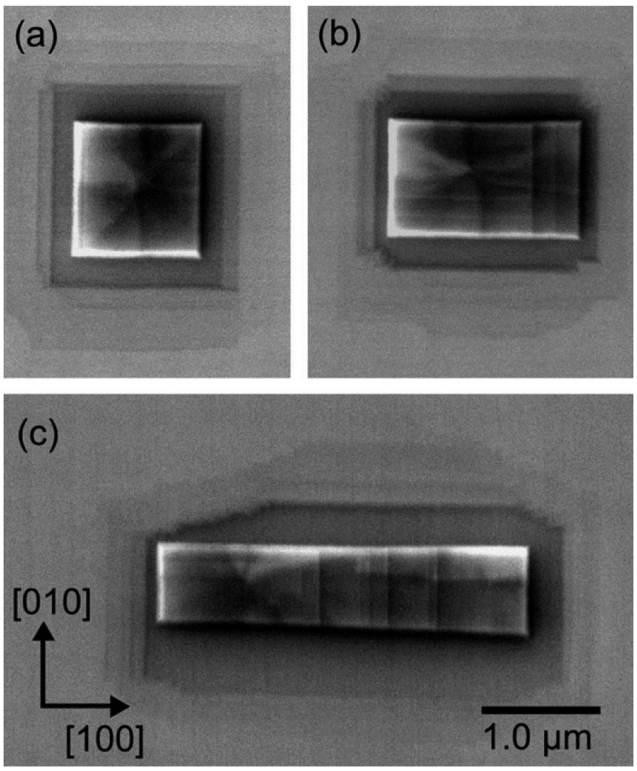

Fig. 11 Scanning electron micrograph (SEM) image of epitaxial islands of the anatase polymorph of TiO_2 that form on top of $SrTiO_3(001)$. Square islands, shown in (a), narrow in width and elongate in length (as shown in (b) and (c)), at a critical width of 1.3 μm. Reprinted figure with permission from [M. S. J. Marshall and M. R. Castell, *Phys. Rev. Lett.*, 2009, **102**, 146102]. Copyright (2009) by the American Physical Society.[30]

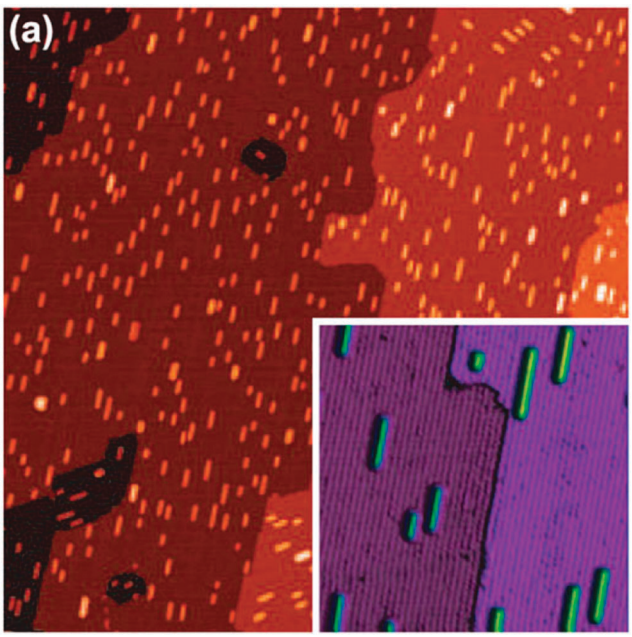

Fig. 12 Ag nanoislands on Si(111)-(4 × 1) (381 × 381 nm^2). Inset image is a high-resolution 3D rendering of the Ag nanowires (64 × 64 nm^2, $V_s = -2.0$ V, $I_t = 20$ pA). Reprinted figure with permission from [A. Li *et al. Phys. Rev. Lett.*, 2009, **103**, 076102]. Copyright (2009) by the American Physical Society.[37]

6. STM examples of self-assembled oxide nanostructures

6.1 Nanostructured $SrTiO_3(001)$

When $SrTiO_3$ is annealed in reducing conditions, as in ultra-high vacuum, Ti and O gradually segregate to the surface forming a TiO_x-rich surface. This results most notably in a family of epitaxial linear TiO_x-rich nanostructures on the $SrTiO_3(001)$ surface. An isolated 12 nm long line is shown in Fig. 13 where the spots that form the nanoline can be seen. Because the nanoline is comprised of two rows of spots, it is termed a diline. The spots in a row are separated by 0.8 nm, corresponding to twice the lattice constant of $SrTiO_3(001)$. Prolonged annealing of $SrTiO_3(001)$ results in the formation of close-packed domains of dilines with a periodicity of (6×2).[38]

Determining the chemical composition of the nanostructures is a necessary but often insufficient step to determining the structure. As computing power has increased, first principles calculations can provide information about the surface structure. Using experimental results as a starting point, first principles density functional theory (DFT) can be used to test structures and simulate scanning tunnelling microscopy images for comparison with experimentally acquired images. The structures calculated using DFT reach a global minimum for the proposed structure. With experimental input, a variety of structures can be tested and compared with experiment. Wide-spread simulation of STM images and comparison to experiment has proven to be an effective way of accurately determining the atomic structure of a nanostructure in a way that would be difficult using purely experimental methods. *Ab initio* calculations of the TiO_x dilines reveal that each spot corresponds to a complex of Ti and O atoms that appear in STM images as a single spot, referred to as a polyhedral quartet motif. This is a shared structural unit found in $c(4 \times 2)$ reconstructions and among the other linear nanostructures.[6] This structure is shown top-down and in side-view in Fig. 14(a). STM simulations of the structure show agreement

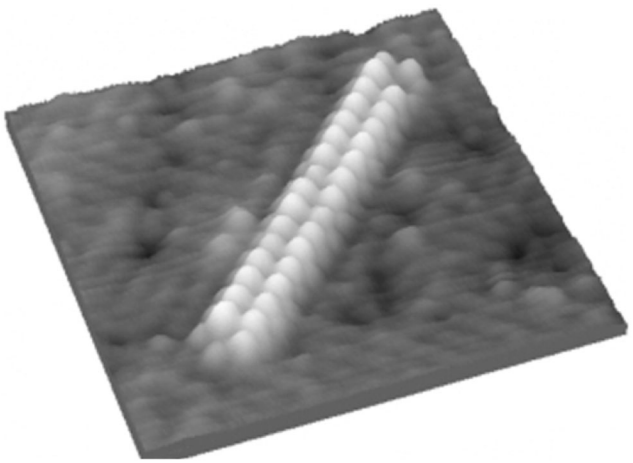

Fig. 13 A high magnification 3D rendering of a STM image that depicts a TiO_x diline that has formed on the surface of $SrTiO_3(001)$ (14 × 14 nm^2). Image adapted from Castell.[40]

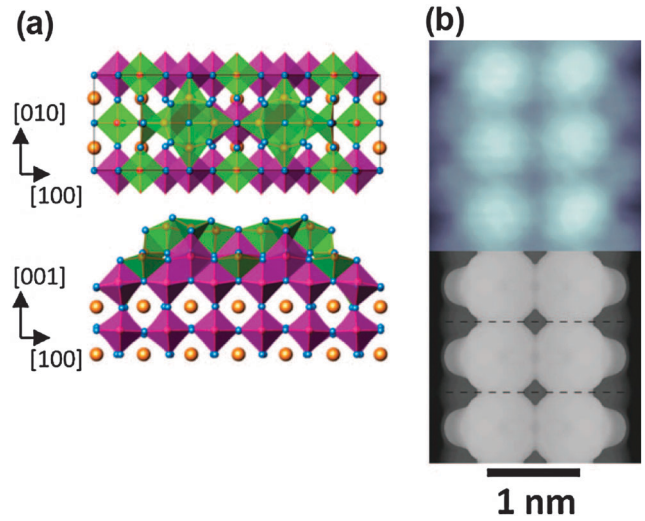

Fig. 14 *Ab initio* calculations of the structure of a diline in (a), where orange-coloured atoms are Sr, blue atoms are O, and red atoms are Ti. Purple octahedra are fully coordinated Ti–O octahedral, while the green denotes partially coordinated Ti–O octahedra. A comparison of an STM simulation (bottom panel) with an experimental STM image (top panel) is shown in (b). Reprinted with permission from [A. E. Becerra-Toledo *et al.*, *J. Chem. Phys.*, 2012, **136**, 214701]. Copyright (2012), AIP Publishing LLC.[6]

with experimental STM images in Fig. 14(b). The nucleation and growth of the dilines were observed over 24 minutes using high-temperature STM at temperatures of 800 °C.[39] Stable nucleation centres contain two parallel rows that have a length of at least three bright spots each, as shown in Fig. 15.

The width of the nanolines can be either 2, 3 or 4 $SrTiO_3$ unit cells wide, and as such are termed dilines, trilines and tetralines respectively. An STM image of a (6 × 2) close-packed domain of dilines is shown in Fig. 16(a). The stoichiometry of the nanoline changes as the width increases. A nanoline that is 3 unit cells wide is a triline and when found in close-packed domains has an (8 × 2) periodicity, as in Fig. 16(b). The centre row of the triline often appears in STM images as brighter than the side rows. The brightness of this central row can also be changed by changing the sample bias voltage. Since STM is a convolution of the local density of states and the surface structure, this indicates that the centre row of a triline has a higher local density of states, and increased metallicity. Auger electron spectroscopy has been used on $SrTiO_3$ samples covered in nanolines and compared with a stoichiometric sample.[38] An enhanced Ti peak is observed for the nanoline samples which allows one to infer that they are TiO_x rich. The nucleation and growth of trilines was observed by 'hot STM' and revealed two adjacent dilines forming into a single triline. Nanolines that are 4 unit cells in width (called tetralines) have a periodicity of (12 × 2) when found in close-packed domains as shown in Fig. 16(c).

Three other nanostructures can also form on $SrTiO_3$(001) including metadilines [Fig. 16(e)] – a degenerated form of dilines, cross-dots [Fig. 16(f)] and waffle structures [Fig. 16(d)]. The cross-dots form close-packed (7 × 4) domains, while the waffles form close-packed (6 × 8) domains. These three remaining

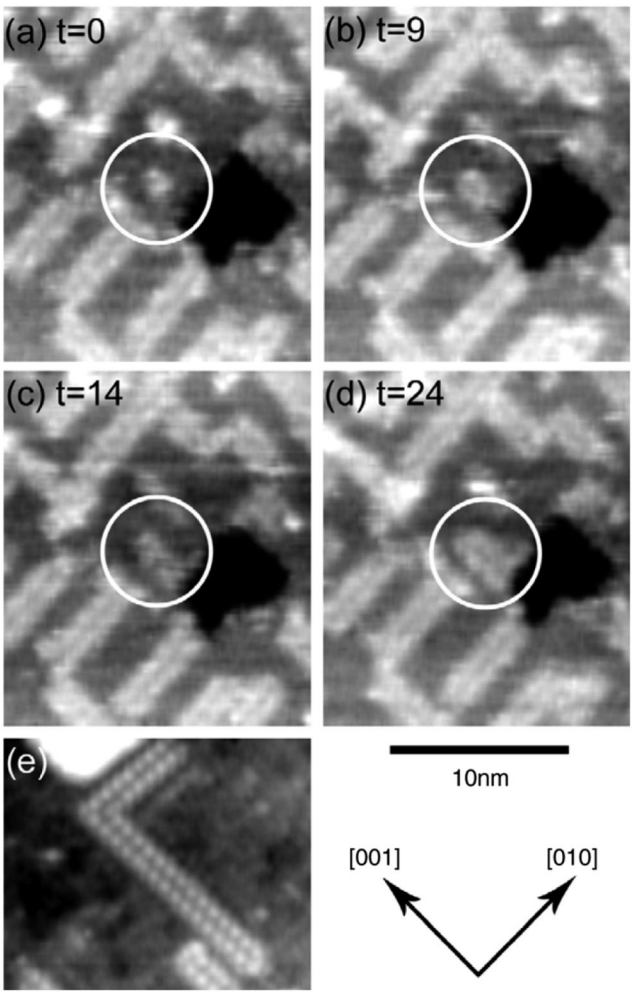

Fig. 15 STM images taken at 800 °C over 24 minutes that show the formation and growth of a stable diline nucleation centre for a diline (circled in white) in (a)–(d) (V_t = 2.0 V, I_t = 0.1 nA). Fully-formed dilines decorating the surface of $SrTiO_3$(001) are shown in (e) (V_t = 1.1 V, I_t = 0.1 nA). Copyright IOP Publishing. Reproduced by permission of IOP Publishing. All rights reserved.[39]

nanostructures are also found oriented along the ⟨001⟩ directions. While the epitaxial nanostructures depicted in Fig. 16 bear some similarity to surface reconstructions, they are more aptly termed ordered nanostructures since it is possible for these structures, particularly the nanolines, to appear in isolation rather than close-packed domains. These nanostructures can be used for templated growth of molecules[42] or nanocrystals, and may also have interesting catalytic properties.

6.2 Nanostructured $SrRuO_3$

The appearance of linear nanostructures have recently also been observed on $SrRuO_3$(001), grown *via* pulsed laser deposition on $SrTiO_3$(001). These nanolines are shown in Fig. 17, and at first glance the nanolines have a similar appearance to the dilines observed on $SrTiO_3$. However, the dimensions of the nanolines on $SrRuO_3$ and the orientation relative to the substrate are markedly different than the nanolines observed on $SrTiO_3$. Using *ab initio*

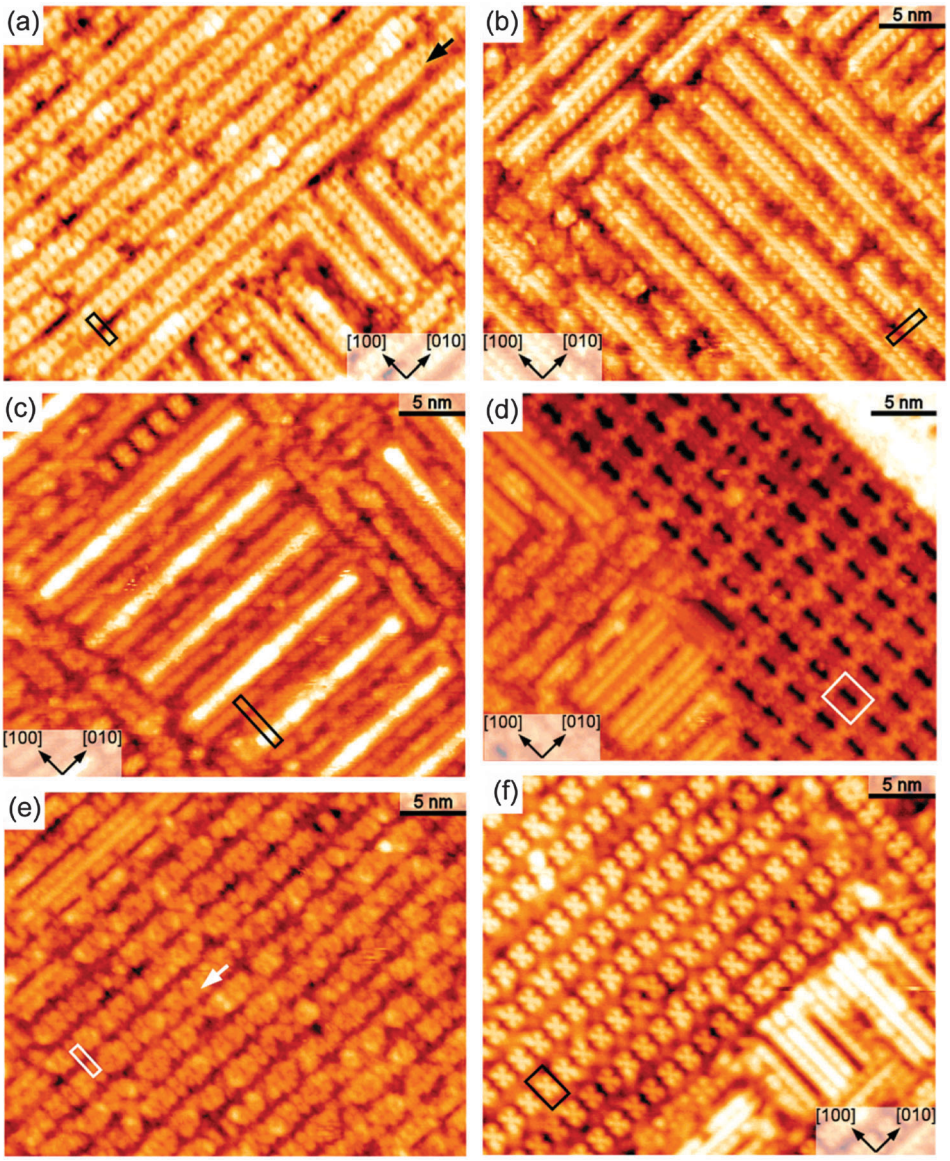

Fig. 16 Nanostructured TiO_x-rich $SrTiO_3$(001) surfaces. (a) Dilines, which can form (6 × 2) close-packed domains. (b) (8 × 2) trilines, (c) (12 × 2) tetralines, (d) (6 × 8) waffles, (e) (6 × 2) meta-dilines and (f) (7 × 4) cross-dots. Adapted from Deak.[38,41]

modelling, Tselev *et al.* showed that the nanolines that decorate the surface of $SrRuO_3$ are adsorbed oxygen atoms that decorate the surface in a regular way.[43] Similar to the nanolines found on $SrTiO_3$, the constituent dots of the nanolines on $SrRuO_3$ can also be found in zig-zag and rectangular configurations. However, the dramatically different chemical structures of the nanolines on $SrTiO_3$ and $SrRuO_3$ despite the similar appearances demonstrate the need for DFT modelling to deconvolve the LDOS and structure.

7. STM examples of other epitaxial nanostructures

In the preceding section, we described the formation of self-assembled linear nanostructures atop perovskite oxides. These nanostructures form as a result of *in situ* sputtering and annealing of $SrTiO_3$, as well as following deposition of $SrRuO_3$ with pulsed laser deposition. Use of STM to study epitaxial nanostructures extends far beyond the perovskite oxides to include virtually every relevant conductive material. In this section, we will briefly discuss three examples of epitaxial nanostructures in different materials systems, all of which suggest future directions for the field.

7.1 Self-assembled metal nanoislands

In the Stranski–Krastanov growth mode, strain in an epitaxial overlayer is relieved *via* the formation of islands. Alternatively, ultrathin strained epitaxial layers can relieve the strain *via* the formation of ordered networks of dislocations. The energy of the dislocations are different than the energy of the surface, which has implications for the nucleation and growth of additional material. For instance, in Fig. 18, an STM image

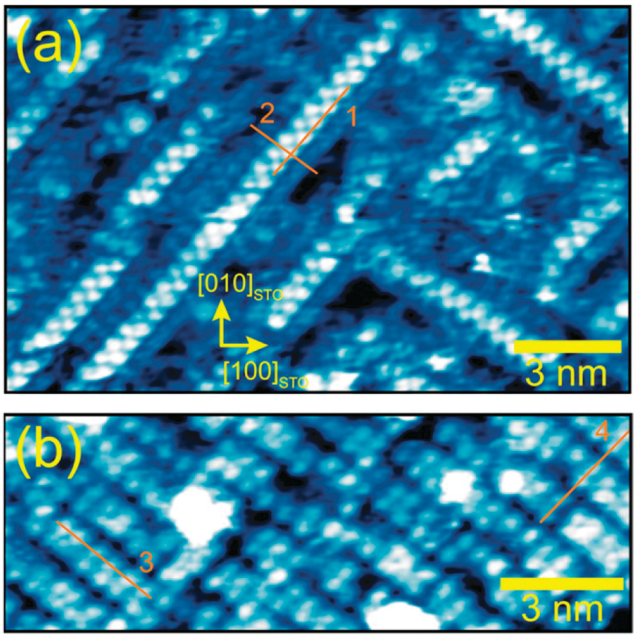

Fig. 17 (a) Zig-zag nanoline structures are shown in (a) (V_t = 1.4 V, I_t = 25 pA) and rectangular nanostructures are shown in (b) (V_t = 1.6 V, I_t = 150 pA). Reprinted with permission from [A. Tselev *et al.*, *ACS Nano*, 2013, **7**, 4403]. Copyright (2013) American Chemical Society.[43]

shows a periodic array of triangularly shaped Fe nanoislands.[44] The nanoislands are grown atop a bilayer of strained copper that was deposited onto the (111) face of Pt. To relieve strain, a network of dislocations forms in the copper bilayer. The dislocations repel adatoms of Fe that preferentially nucleate on dislocation-free areas of the surface. The result is a periodic array of Fe nanoislands. In this way, strain-relief in a 2 monolayer thick film of Cu can be used to engineer the formation of an ordered array of Fe nanoislands, an approach that has been extended to other metals.

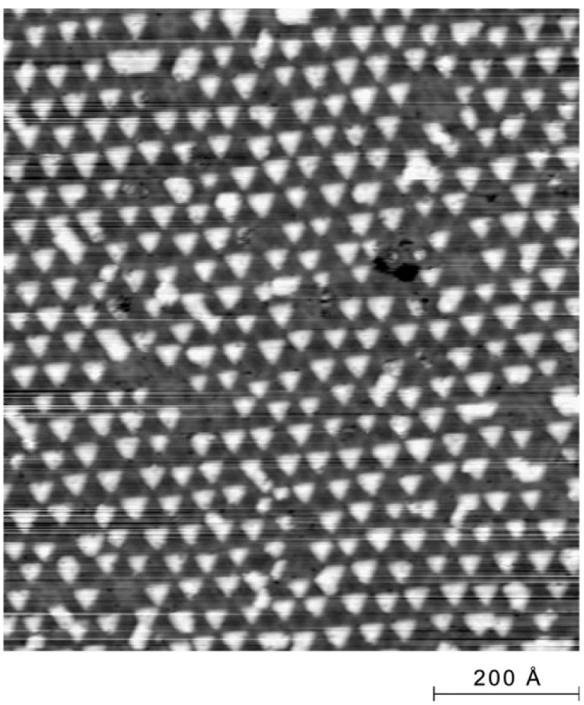

Fig. 18 STM images of an array of Fe islands grown on a Cu bilayer atop Pt(111) at 250 K.[44] Reprinted by permission from Macmillan Publishers Ltd: [*Nature*] H. Brune *et al.*, *Nature*, 1998, **394**, 451.

7.2 Epitaxy of supramolecular networks

Thus far, our discussion has focused on epitaxy of crystalline materials. However, a field has emerged in which large molecules deposited onto surfaces self-assemble into ordered structures. Because these networks are commensurate with the surface, it is appropriate to consider these as epitaxial nanostructures. By controlling the size and chemical terminations of the molecules, a variety of patterns can be formed. For instance, Fig. 19(a) shows an STM image of a supramolecular network composed of perylene tetra-carboxylic di-imide (PTCDI) and melamine, and grown atop Ag/Si(111)-$\sqrt{3} \times \sqrt{3}$R30°. Inset in Fig. 19(a) is an atomic resolution image of the underlying surface where a hexagon denotes the schematic representation of the substrate. The PTCDI and melamine form an open honeycomb structure, which is potentially useful for deposition of molecules such as fullerenes or for creating preferential

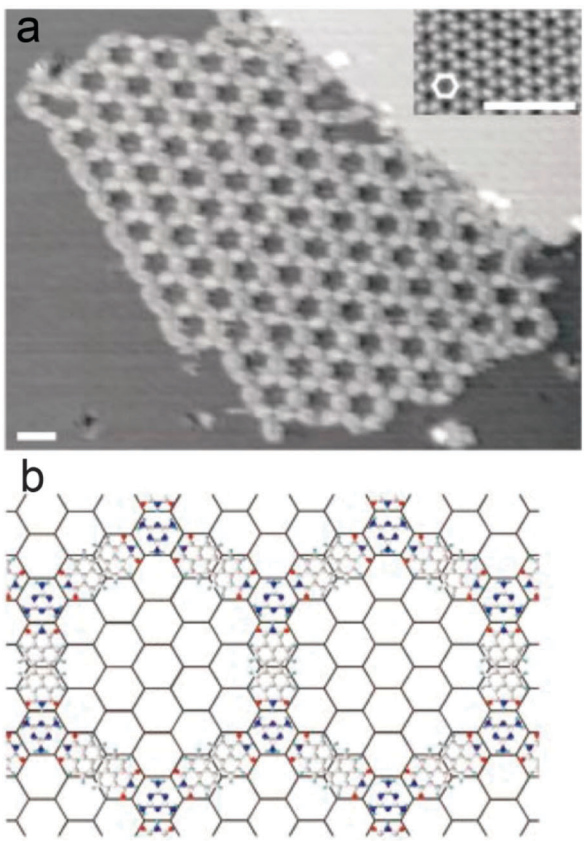

Fig. 19 (a) STM image of a self-assembled array of PTCDI-melamine supramolecular network grown on Ag/Si(111)-$\sqrt{3} \times \sqrt{3}$R30°. (b) A schematic that shows the registry of the supramolecular network with the surface, where the surface is represented by a hexagonal network. Reprinted by permission from Macmillan Publishers Ltd: [*Nature*] J. Theobald *et al.*, *Nature*, 2003, **424**, 1029.[45]

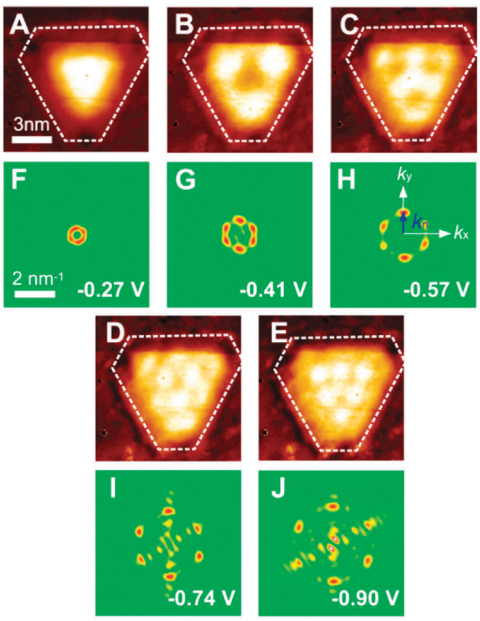

Fig. 20 d*I*/d*V* maps (A–E) and the corresponding Fourier transform maps (F–J) obtained from an epitaxial island of graphene grown on Ir(111). Reprinted with permission from Phark *et al.*[46]

binding sites.[45] Fig. 19(b) shows the registry of the supramolecular network with the hexagonal lattice of the substrate.

7.3 STM-spectroscopy of epitaxial graphene

One of the most exciting emerging fields in materials science focuses on the growth of epitaxial graphene. In order to answer the question of how the electronic structure of graphene changes as a function of size at the nanoscale, Phark *et al.* used energy-resolved d*I*/d*V* maps in order to probe the electronic structure of graphene grown epitaxially on Ir(111) as shown in Fig. 20(A)–(E).[46] Taking the Fourier transform of the d*I*/d*V* map, as shown in Fig. 20(F)–(J) enables the determination of the wave vectors, which ultimately can be used to determine the standing wave pattern in the 2D nanostructure. STM has been very effectively used in this manner on single crystals,[47] and extending this work to nanostructured materials is an important way of elucidating the relationship between size and electronic structure of an epitaxial nanostructure. This is of particularly importance in the study of 2D nanomaterials.

8. Conclusions and outlook

The formation and growth of epitaxial nanomaterials are intimately linked to the atomic structure of both the substrate, and the materials under study. STM is an invaluable tool for determining the atomic structure of a conductive material and for providing insight into the formation and growth of islands at the nanoscale. The ability of STM to probe the local density of states has provided valuable insight into the origin of catalytic properties. Nonetheless, proper interpretation of atomic resolution STM images is critically important, and understanding what is observed in these images through the use of image simulations is crucial.

The outlook for using STM to study epitaxial nanostructures is positive. Advances in instrumentation have improved spatial control and stability at the nanoscale such that the tip can be used to locally manipulate nanostructures, or can be used to lithographically define features. Self-assembly of nanostructures can create densities that exceed lithographic techniques at smaller length scales. Moreover, combining the high spatial resolution of STM with tunnelling spectroscopy facilitates probing the electronic structure of materials at a fundamental level.

Notes and references

1 M. R. Castell, in *Nanocharacterisation*, ed. J. Hutchison and A. Kirkland, RSC Publishing, 2007, pp. 66-93.
2 R. J. Hamers, *Annu. Rev. Phys. Chem.*, 1989, **40**, 531–559.
3 J. Tersoff and D. R. Hamann, *Phys. Rev. B: Condens. Matter Mater. Phys.*, 1993, **31**, 805–813.
4 K. Stokbro, U. Quaade and F. Grey, *Appl. Phys. A: Mater. Sci. Process.*, 1998, **66**, S907–S910.
5 C. J. Chen, *Introduction to Scanning Tunneling Microscopy*, Oxford University Press, New York, 1993.
6 A. E. Becerra-Toledo, M. S. J. Marshall, M. R. Castell and L. D. Marks, *J. Chem. Phys.*, 2012, **136**, 214701–214709.
7 R. Wiesendanger, *Scanning Tunneling Microscopy III: Theory of STM and Related Scanning Probe Methods*, Springer, 1993.
8 M. F. Crommie, C. P. Lutz and D. M. Eigler, *Science*, 1993, **262**, 218–220.
9 S. A. Chambers, *Surf. Sci. Rep.*, 2000, **39**, 105–180.
10 J. A. Venables, G. D. T. Spiller and M. Hanbucken, *Rep. Prog. Phys.*, 1984, **47**, 399.
11 W. Winterbottom, *Acta Metall.*, 1967, **15**, 303–310.
12 G. Wulff, *Z. Kristallogr.*, 1901, **34**, 449–530.
13 C. Herring, *Phys. Rev.*, 1951, **82**, 87–93.
14 F. Silly and M. R. Castell, *Phys. Rev. Lett.*, 2005, **94**, 046103.
15 J. V. Lauritsen, J. Kibsgaard, S. Helveg, H. Topsøe, B. S. Clausen, E. Lægsgaard and F. Besenbacher, *Nat. Nanotechnol.*, 2007, **2**, 53–58.
16 S. Helveg, J. V. Lauritsen, E. Lægsgaard, I. Stensgaard, J. K. Nørskov, B. S. Clausen, H. Topsøe and F. Besenbacher, *Phys. Rev. Lett.*, 2000, **84**, 951–954.
17 R. T. Vang, J. V. Lauritsen, E. Lægsgaard and F. Besenbacher, *Chem. Soc. Rev.*, 2008, **37**, 2191–2203.
18 J.-N. Aqua, I. Berbezier, L. Favre, T. Frisch and A. Ronda, *Phys. Rep.*, 2012, **522**, 59–189.
19 B. Daudin, F. Widmann, G. Feuillet, Y. Samson, M. Arlery and J. L. Rouvière, *Phys. Rev. B: Condens. Matter Mater. Phys.*, 1997, **56**, R7069–R7072.
20 K. Yamaguchi, K. Yujobo and T. Kaizu, *Jpn. J. Appl. Phys.*, 2000, **39**, 1245.
21 S. G. Corcoran, G. S. Chakarova and K. Sieradzki, *Phys. Rev. Lett.*, 1993, **71**, 1585–1588.
22 G. Medeiros-Ribeiro, A. M. Bratkovski, T. I. Kamins, D. A. A. Ohlberg and R. S. Williams, *Science*, 1998, **279**, 353–355.

23 Y.-W. Mo, D. E. Savage, B. S. Swartzentruber and M. G. Lagally, *Phys. Rev. Lett.*, 1990, **65**, 1020–1023.
24 I. Goldfarb, P. T. Hayden, J. H. G. Owen and G. A. D. Briggs, *Phys. Rev. Lett.*, 1997, **78**, 3959–3962.
25 O. E. Shklyaev, M. J. Beck, M. Asta, M. J. Miksis and P. W. Voorhees, *Phys. Rev. Lett.*, 2005, **94**, 176102.
26 A. Rastelli, M. Stoffel, G. Katsaros, J. Tersoff, U. Denker, T. Merdzhanova, G. S. Kar, G. Costantini, K. Kern, H. von Känel and O. G. Schmidt, *Microelectron. J.*, 2006, **37**, 1471–1476.
27 A. Li, F. Liu and M. G. Lagally, *Phys. Rev. Lett.*, 2000, **85**, 1922–1925.
28 I. Goldfarb, *Surf. Sci.*, 2007, **601**, 2756–2761.
29 J. Tersoff and R. M. Tromp, *Phys. Rev. Lett.*, 1993, **70**, 2782–2785.
30 M. S. J. Marshall and M. R. Castell, *Phys. Rev. Lett.*, 2009, **102**, 146102.
31 O. L. Alerhand, D. Vanderbilt, R. D. Meade and J. D. Joannopoulos, *Phys. Rev. Lett.*, 1988, **61**, 1973–1976.
32 V. Marchenko and A. Y. Parshin, *Sov. Phys. JETP*, 1980, **52**, 129–131.
33 L. D. Landau, L. P. Pitaevskii, A. M. Kosevich and E. M. Lifshitz, *Theory of Elasticity*, Butterworth-Heinemann, 1984.
34 M. S. J. Marshall, DPhil thesis, University of Oxford, 2009.
35 Z. He, M. Stevens, D. J. Smith and P. A. Bennett, *Surf. Sci.*, 2003, **524**, 148–156.
36 F. Silly and M. R. Castell, *Appl. Phys. Lett.*, 2004, **85**, 3223–3225.
37 Y. Li, M. Liu, D. Ma, D. Yu, X. Chen, X.-C. Ma, Q.-K. Xue, K. Xu, J.-F. Jia and F. Liu, *Phys. Rev. Lett.*, 2009, **103**, 076102.
38 D. S. Deak, F. Silly, D. T. Newell and M. R. Castell, *J. Phys. Chem. B*, 2006, **110**, 9246–9251.
39 H. L. Marsh, D. S. Deak, F. Silly, A. I. Kirkland and M. R. Castell, *Nanotechnology*, 2006, **17**, 3543–3548.
40 M. R. Castell, *Surf. Sci.*, 2002, **516**, 33–42.
41 D. S. Deak, DPhil thesis, University of Oxford, 2007.
42 D. S. Deak, F. Silly, K. Porfyrakis and M. R. Castell, *J. Am. Chem. Soc.*, 2006, **128**, 13976–13977.
43 A. Tselev, P. Ganesh, L. Qiao, W. Siemons, Z. Gai, M. D. Biegalski, A. P. Baddorf and S. V. Kalinin, *ACS Nano*, 2013, **7**, 4403–4413.
44 H. Brune, M. Giovannini, K. Bromann and K. Kern, *Nature*, 1998, **394**, 451–453.
45 J. A. Theobald, N. S. Oxtoby, M. A. Phillips, N. R. Champness and P. H. Beton, *Nature*, 2003, **424**, 1029–1031.
46 S.-H. Phark, J. Borme, A. L. Vanegas, M. Corbetta, D. Sander and J. Kirschner, *ACS Nano*, 2011, **5**, 8162–8166.
47 J. E. Hoffman, K. McElroy, D.-H. Lee, K. M. Lang, H. Eisaki, S. Uchida and J. C. Davis, *Science*, 2002, **297**, 1148–1151.